Macromolecules

pubs.acs.org/Macromolecules Article

Effect of Graft Length and Matrix Molecular Weight on String Assembly of Aligned Nanoplates in a Lamellar Diblock Copolymer

Christian Tabedzki,[⊥] Nadia M. Krook,[⊥] Christopher B. Murray, Russell J. Composto,* and Robert A. Riggleman*

Cite This: *Macromolecules* 2022, 55, 3166–3175 Read Online

ACCESS | Metrics & More | Article Recommendations | Supporting Information

ABSTRACT: Grafted nanoparticle polymer composites have been used to create a highly bespoke class of materials, with spherical nanoparticles serving as the gateway design into this class. Grafted nanoplates (nanoparticles where the radius is longer than the height of the particle) provide opportunities and pathways to control overall system properties through their anisotropic properties. Current research on addressing the challenges associated with assembly is quite limited and unexplored. Using hybrid particle/self-consistent field theory (hSCFT) simulations, we build upon our previous work examining polyethylene glycol (PEG) grafted nanoplates within a nearly symmetric ($f \approx 0.5$) lamellar poly(styrene-*b*-methyl methacrylate) (PS-*b*-PMMA) block copolymer (BCP) matrix. We examine the interplay between the nanoplate graft length and matrix molecular weight and their effect on the potential of mean force (PMF). Ultimately, we discover that the location and depth of both the energetic well (local minimum) and the energetic barrier (local maxima) of the PMF, as well as the existence of the local maxima, are dependent on the relative width of the nanoplates to the lamellar domain, with the longer grafts experiencing deeper energetic wells and further interplate separation distances. The results are driven by the interfacial tension due to the local domain bulging effects caused by the insertion of the nanoplates into the lamellar system. With experimental separation distances of a PEG-grafted gadolinium trifluoride doped with ytterbium and erbium, GdF3:Yb/Er (20/2 mol %) nanoplates corroborate the correlation found in the simulations between larger matrix domains and a widening of the energetic well. Additionally, the average separation distance follows a trend similar to the hSCFT data. We anticipate these results to help in the development and design of anisotropic nanoparticles within BCPs to create nanocomposites tailored for specific applications and properties.

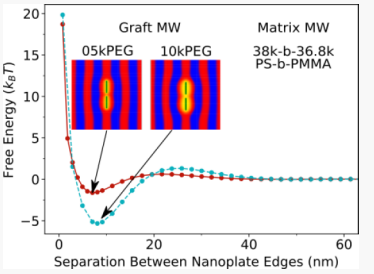

INTRODUCTION

Polymers dominate our everyday life and are constantly pushing the boundaries of modern technology, for example, from aiding in drug delivery[1−4] to safe laxatives[5] to novel purposes like flexible displays for mobile devices.[6] Block copolymers (BCPs), which are polymers made up of multiple blocks of repeating chemical base units, and polymer nanocomposites with BCP matrices show promise for industrial and commercial applications, such as CO_2 separation,[7] stretchable electronics,[8] biomedical implants and tissue engineering,[9] rechargeable batteries,[10] and improved multiferroic devices.[11]

Impregnating a BCP matrix with nanoparticles augments the basic properties of the polymer matrix with the ability to direct heat and mass transport;[12,13] provides magnetic properties;[14−16] and improves the mechanical properties, such as Young's modulus.[17,18] Nanoparticle assembly and properties can also be controlled via stimuli, such as heat and light providing control and tunability.[19] Additionally, grafted nanoparticles can be used to stabilize high-energy lamellar formations by swelling grain boundary structures, thus providing relief to part of the BCP formation.[20] Given the ability to template nanoparticle (NP) assembly, it should come as no surprise that exploration, improvement, and refinement of block copolymer nanocomposite systems are active research areas.

In general, mechanical properties of nanocomposites depend on the size, shape, loading, and dispersion state of the nanoparticle in question,[21−23] including the Young's modulus and tensile strength.[24] Therefore, the future of nanocomposites depends not only on the ability to control nanoparticle dispersion, position, and orientation for a variety of nanoparticles but also on understanding the challenges and interplay that arise when dealing with specific nanoparticle sizes, shapes, and aspect ratios, whether on an absolute length scale or in relation to the host polymer matrix. The positions of nanoparticles within these materials are controlled by manipulating a variety of system parameters, such as matrix molecular weight, chemical composition, graft chain length and

Received: December 2, 2021
Revised: February 28, 2022
Published: April 4, 2022

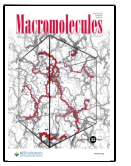

https://doi.org/10.1021/acs.macromol.1c02478
Macromolecules 2022, 55, 3166−3175

graft density, and volume fraction of and size of nanoparticles. However, most of the current knowledge of polymer nanocomposites focuses on isotropic (spherical) nanoparticles that provide a convenient angular symmetry to the system. Using a mix of Monte Carlo simulations and experiments, Akcora et al. were able to display anisotropic self-assembly of spherical, polystyrene-grafted nanoparticles dispersed into a polystyrene homopolymer matrix, with different morphologies of nanoparticle clusters emerging as a function of graft chain density and graft chain length.[25] Likewise, Xu et al. demonstrated, through self-consistent field theory simulations, graft chain length and density affect the relative location of PS-grafted gold nanoparticle within poly(styrene-*b*-2-vinylpyridine) BCP so the particles selectively reside within specific polymer phases or along the interfaces,[26] while Gao et al. used molecular dynamics simulations to show that the location of the grafted NPs in AB diblock lamellae is dependent on the grafting density and interaction strength between the grafts and the A domain.[27] Anisotropic nanoparticles (rods[28,29] and plates[30−32]) can be used to provide orientation-dependent properties, similar to how a cylinder can easily roll along its side like a sphere but resists pivoting about its base like a cube. Nanorods, whose collective properties are affected by the spatial arrangement and macroscopic alignment, can form networks and nanorod arrays that are parallel to BCP microdomains, allowing for morphological control for the production of optical and electronic nanodevices.[28] Example consumer uses for anisotropic materials and properties include thermal heat dissipation from electronics[33,34] and increased shelf life of food via nanocomposite food packaging by reducing the oxygen permeability.[35−38] Understanding what controls the interactions between anisotropic nanoplates is thus of significant importance for controlling the properties of polymer nanocomposites.

Building upon our previous polymer nanocomposite work, this paper focuses on stringing effects of PEG-grafted nanoplates within the attractive PMMA lamellae and explores the contributions of graft molecular weight and matrix molecular weight. Our hybrid particle/self-consistent field theory (hSCFT) simulations are used to visualize the changes of domain bulging and chain compression caused by the introduction of nanoparticles as predicted by Bockstaller et al.,[39] that are unresolvable using classical transmission election microscopy (TEM) techniques. TEM allows us to visualize interplate spacing as a function of matrix molecular weight, complementing one aspect of our simulations. Together, the simulations and TEM figures show that when the nanoplates occupy a larger volume within the lamellar domains, either through reducing the total volume via a smaller matrix (and thus a smaller domain) or through enlarging the nanoplate with longer grafts, the system has a deeper energetic well when the nanoplates are close to each other. Additionally, the larger domains and the larger graft lengths encourage a further equilibrium separation distance. Overall, this knowledge provides insights that can help the development of anisotropic polymer nanocomposites by tailoring properties to selectively promote nanoparticle stringing.

RESULTS AND DISCUSSION

Simulations Analysis. Like in our previous paper,[40] we focus on the emergence of interplate assemblies and the anticipated domain distortion as a result of polymer chain stretching around the grafted nanoplates. We designed our experiments to match to a collection of three experimental lamellar forming block copolymer matrix weights to determine the effect of the molecular weight on the potential of mean force (PMF) and corroborate the simulations: (1) M_n = 38k-*b*-36.8k g/mol, (2) M_n = 95k-*b*-95k g/mol, and (3) M_n = 133k-*b*-130k g/mol lamellar-forming poly(styrene-*b*-methyl methacrylate) (PS-*b*-PMMA) block copolymers (BCPs), with an experimental grafting density of 0.62 chains/nm^2. These matrix molecular weights will be referred to throughout the paper as 38kBCP, 95kBCP, and 133kBCP, respectively. Likewise, we use two graft lengths in our simulations designed to represent M_n = 5 kg/mol and M_n = 10 kg/mol (referred to 5kPEG and 10kPEG, respectively), though only M_n = 5 kg/mol grafted PEG−PO_3H_2 was performed experimentally (referred herein as 5kPEG). We note that the 38kBCP with 5kPEG system was originally studied in our previous paper and has been recasted here for easier comparison.[40] Skeletal representations of the polymers used can be found in Figure 1. To understand

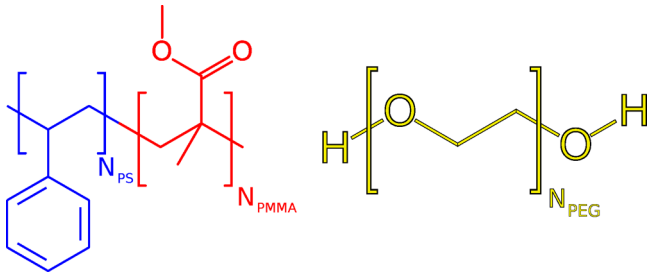

Figure 1. PS-*b*-PMMA diblock matrix (blue and red, respectively) and PEG grafts (off-yellow) chemical representations. These structures are color-coded to match Figure 2.

nanoplate distribution, simulations were performed with two grafted nanoplates inserted into the center of the PMMA domain. Prior studies investigated the effect of plate tilt angle, finding that angles less than 5° are energetically favorable,[40] which was consistent with experimental findings.[41]

The hSCFT algorithm and the Flory−Huggins parameters used here are the same as our previous paper:[40] generally, the χ is the Flory−Huggins parameter and represents the chemical dissimilarity and repulsion between the materials for when χ is positive (negative values of χ represent chemical attraction). Because the PEG grafts have a negative χ interaction with the PMMA domain, we are not only able to tailor the design of the material and control the location of the nanoplates within the system but also are able to improve the solubility of the particles within the matrix. In addition to the Flory−Huggins interactions, all polymers and nanoparticles contribute to the overall density of the system; a constant density throughout the box is ensured via Helfand compressibility interactions. Due to the high grafting density which shields the NP, the only nanoparticle−polymer interactions are the Helfand compressibility interactions, and the energy differences between the particle and polymers are assumed to be negligible. A comprehensive description of the methods, materials, and numerical parameters can be found in the Methods section at the end of the paper. We also refer the reader to our previous paper and its corresponding Supporting Information for a more in-depth explanation of the simulation technique and the semi-implicit Euler update scheme.[40]

Looking at the visualizations of the energetic minima of the system in Figure 2, one systematic difference is the domain size

https://doi.org/10.1021/acs.macromol.1c02478
Macromolecules 2022, 55, 3166−3175

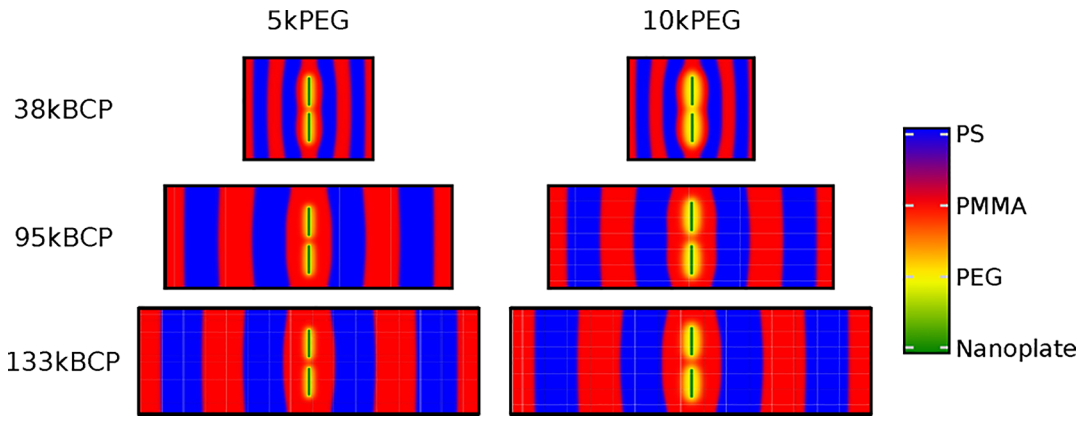

Figure 2. 2D snapshots for each energetic minima of 5k and 10k g/mol PEG-grafted nanoplates in BCP matrices with molecular weights of 38k, 95k, and 133k g/mol. The figures are cropped vertically but are uncropped horizontally to allow comparisons between the periodic width and interfacial deformations. These figures are scaled to the size of the nanoplate. The heat map shows the location of PS and PMMA, in the BCP, PEG brush, and nanoplate.

Table 1. Model Parameters for Each Simulation Performed

system ID	38kBCP−5kPEG	95kBCP−5kPEG	133kBCP−5kPEG	38kBCP−10kPEG	95kBCP−10kPEG	133kBCP−10kPEG
N_{PS}	30	75	105	30	75	105
N_{PMMA}	30	75	105	30	75	105
N_{PEG}	9	9	9	16	16	16
$\chi_{PS-PMMA}$	0.501604	0.5017	0.50172	0.501604	0.5017	0.50172
χ_{PS-PEG}	1.13437	1.13437	1.13437	1.27847	1.27847	1.27847
$\chi_{PMMA-PEG}$	−0.01821	−0.01821	−0.01821	−0.020522	−0.020522	−0.020522
box width by length (b units)	52.0 × 90	112.4 × 90	138.84 × 90	52.0 × 90	112.4 × 140	138.84 × 140
collocation points	525 × 875	1029 × 875	1323 × 875	525 × 875	1029 × 1323	1323 × 1323

in the horizontal direction. (The figures have been trimmed to have the same subsection of the vertical dimension shown; the simulations are designed to have the same nanoplate core size, which serves as a reference length scale. The simulations extend further than what is shown; full box dimensions can be found in Table 1.) Naturally, as the molecular weight of the polymer matrix increases from 38kBCP to 133kBCP, the domain spacing increases for both 5kPEG and 10kPEG cases; interestingly, this does not appear to have an effect on how many interfacial periods are distorted by the insertion of nanoplates with minimal distortion for the furthest interface shown. Namely, only the two nearest PMMA domains are significantly distorted to accommodate the PS domain adjacent to the plate-filled PMMA domains. Like the domain spacing, the differences in the interfacial distortions in the filled PMMA domains are visibly apparent: at each BCP weight, the bulge for the smaller graft (5kPEG) is noticeably smaller than for the larger 10kPEG.

Overall, competing effects in this system emerge from the lengths of the grafted chains and of the BCP, with the volume fraction of the grafted nanoplate serving as a useful proxy for understanding these effects. A nanoplate that takes up a larger volume fraction distorts the interface more. Because a longer graft chain distorts the interface more for a given domain size, one would expect a longer graft chain to have a higher energetic barrier, due to the increased curvature on the interfacial surface. Similarly, one would also expect a deeper energetic well as the two interfacial bulges combine into one. For a given graft length, as the matrix molecular weight increases, the domain size increases, reducing the overall impact of the nanoplates on the interfacial domain as they occupy less volume and are no longer located near the interface; in the limit of sufficiently large domains, the nanoplates will have negligible contributions. Thus, the energetic well should approach an asymptotic point where the depth of the well is dominated by the interactions between the grafted nanoplates themselves and not the host component of the matrix. Likewise, the energetic barrier should decrease and even disappear completely as the matrix molecular weight increases and the volume fraction of the nanoparticles tends to zero.

We next compare our predictions from the visualizations by examining how the design parameters affect the potential of mean force (PMF) graphs. We begin our analysis with plots showing the effect of the graft length and the BCP molecular weight simultaneously to highlight the interplay before isolating the effects of the individual parameters. Figure 3 shows the free energy versus nanoplate separation for the 38k and 95k block copolymer matrices for both PEG graft lengths. We chose to exclude the 133k block copolymer systems from this analysis since the largest change is between 38k and 95k block copolymer matrices, as will be demonstrated. We note common features between these PMF curves including a precipitous penalty at small separation distances representing large chain-overlap (and also unphysical nanoplate-nanoplate overlap); a global minimum representing an energetic well favoring nanoparticle aggregation emanating from depletion-attraction interactions; a local maximum at slightly larger distances representing an activated state (or energetic barrier); and finally, a tapering and a plateau as the interaction effects between the nanoplates move beyond the effective interplate interaction range. Our nanoplate−nanoplate interactions bear similarities to hydrophobic interactions of solutes. Small hydrophobic particles do not disrupt water's tetrahedral

https://doi.org/10.1021/acs.macromol.1c02478
Macromolecules 2022, 55, 3166−3175

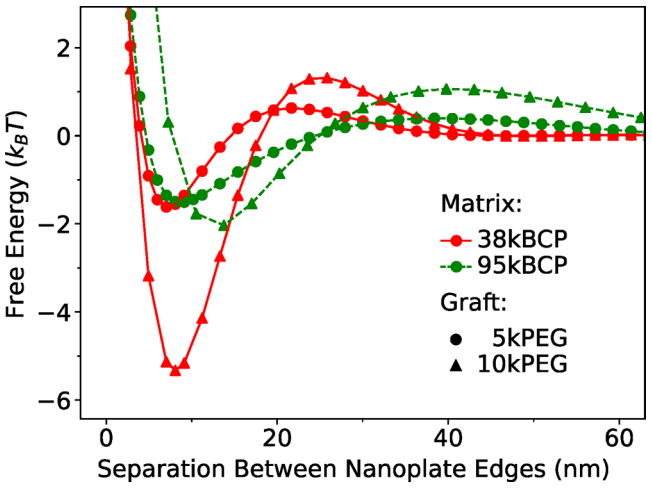

Figure 3. Potential of mean forces as a function of both graft and matrix lengths. The reference energy $F_0 = 0$ is defined as the energy of the simulation box when the center of the nanoplates are one-half box-length away, constrained within the same lamellar domain.

hydrogen bond network as the water molecules can accommodate the particles though with a significant loss of entropy. This restricts the configurations of water in the solute's hydration shell; larger solutes disrupt the hydrogen network similar to a vapor−liquid interface which are more enthalpic in nature.[42] Therefore, the hydrophobic nanoparticles and our nanoplates are similar in that the nanoparticles come together and reduce the PMMA/NP interface. That said, we believe that a majority of the attractive interactions comes from the reduction of the curvature of the interface as well as a reduction in the overall interfacial area, which is necessarily enthalpic in nature.

We also note the significant differences between the shapes of the PMFs. The larger graft within the smaller matrix (38kBCP−10kPEG) has a much deeper energetic well ($\approx -5k_BT$) compared to the other matrix combinations (≈ -2.0, $\approx -1.5k_BT$) because of the relatively large nanoplate (including the grafted chains) occupying the narrow domain and the corresponding interfacial distortion. This system also features a stronger and more pronounced energetic barrier ($\approx 1.3k_BT$) compared to the 38kBCP−5kPEG ($\approx 0.6k_BT$). Similarly, 95kBCP−10kPEG has a deeper energetic well ($\approx -2.0k_BT$) compared to 95kBCP−5kPEG ($\approx -1.5k_BT$) and also features a larger energetic barrier ($\approx 1.1\ k_BT$ vs $\approx 0.4k_BT$). The broader energetic barriers found in the 93kBCP systems, along with the shallower wells, discourage the formation of larger nanoplate chains and encourage nanoplates to separate by relatively long distances. We also note that the trend of the relatively flat and wide energetic barriers exists for the 133kBCP systems, with $\approx 0.0\ k_BT$ and $\approx 0.6\ k_BT$ for 5k and 10kPEG grafts, respectively. These shallow, wide barriers exist at larger molecular weights because the polymer matrices do not experience as much interfacial tension/distortion due to the smaller volume fraction of the grafted nanoplate within the lamellar domain.

Figure 4 allows us to compare the effect of matrix molecular weight at constant graft length. In Figure 4a, the magnitudes of the energetic minima are very similar (≈ 1.5, $\approx 1.6k_BT$) across all matrix molecular weights; the location and the width of the minimum increases slightly as the matrix molecular weight increases (specific values for the minima are available in Table 2). The change in the matrix molecular weight meaningfully affects the location of the energy barrier as two nanoplates are brought together, supporting the hypothesis that the dominant interactions within the observed range for the well are the nanoplate−nanoplate interactions. For 38kBCP, there is a distinct free energy barrier with a maximum located at 23.8 nm. The free energy barrier diminishes in larger domains as the 95kBCP has a much wider barrier peaking at 38.6 nm ($\approx 0.4\ k_BT$), and the 133kBCP barely has a barrier at 53.5 nm ($\approx 0.03\ k_BT$). This difference in the energy profiles comes from the domain spacing and the deformation to the interface mentioned earlier, with the deformation being the main contributing factor to the energetic barrier, supporting the hypothesis that the systems with larger domain sizes (and thus domains with a smaller nanoplate volume fraction) would weaken or possibly eliminate the energetic barrier.

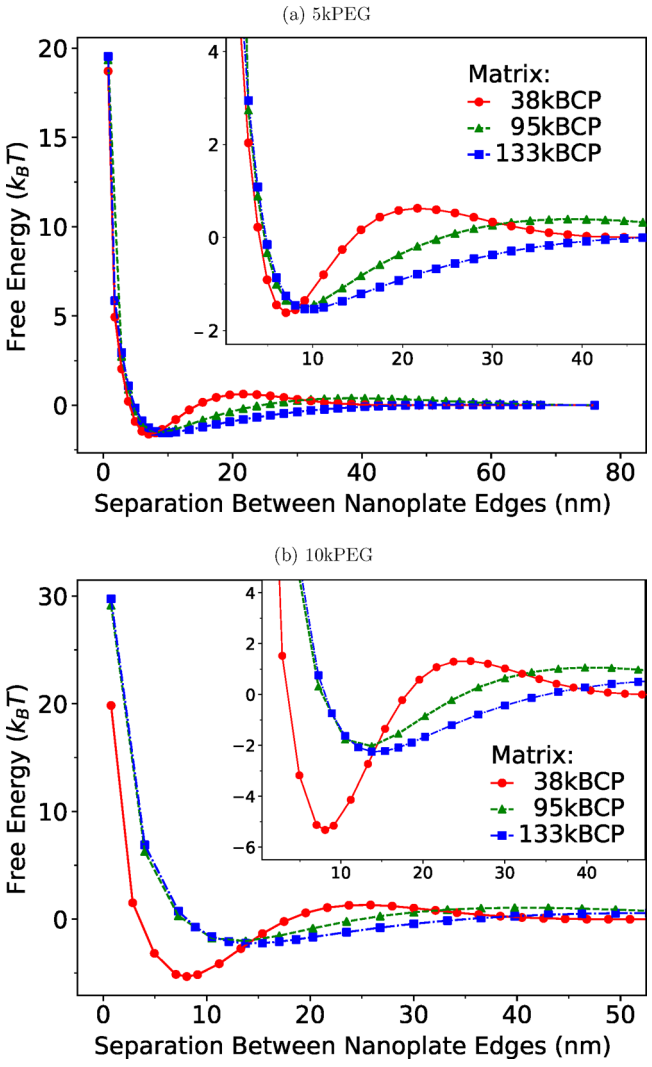

Figure 4. Potential of mean force (PMF) curves to describe free energy as a function of edge-to-edge separation for (a) 5k and (b) 10kPEG-grafted nanoplates in the PMMA domain of PS-*b*-PMMA lamellae for various matrix molecular weights. The insets expand the region near the minima. 38kBCP is colored red, 95kBCP is green, and 133kBCP is blue.

The corresponding matrix molecular weight analysis for 10kPEG grafts is shown in Figure 4b and features a similar trend to the 5kPEG: as the molecular weight of the matrix increases, the nanoplates' relief and contribution to the

https://doi.org/10.1021/acs.macromol.1c02478
Macromolecules 2022, 55, 3166−3175

Table 2. Energetic Barriers and Minima for Each Simulation Performed

System ID	38kBCP−5kPEG	95kBCP−5kPEG	133kBCP−5kPEG	38kBCP−10kPEG	95kBCP−10kPEG	133kBCP−10kPEG
Energetic minimum (k_BT)	−1.62	−1.51	−1.54	−5.33	−2.04	−2.25
Location of minimum (nm)	7.3	8.8	9.7	8.1	13.3	14.2
Energetic barrier (k_BT)	0.63	0.40	0.03	1.32	1.06	0.58
Location of barrier (nm)	21.7	38.5	53.4	25.1	40.5	53.4

energetic well decrease ($\approx -5.3\ k_BT \rightarrow \approx -2.0\ k_BT \rightarrow \approx -2.3\ k_BT$). Additionally, as the two nanoplates approach each other, the excluded volumes begin to overlap; the grafts overlap, reducing the volume available for the matrix chains to occupy, thus reducing the configurations available. The repulsion out of the excluded volume causes the nanoplates to favor coming closer and fully excluding the matrix chains, while simultaneously increasingly interfacial area, leading the energetic well to be a mix of energy increasing interfacial area and energy decreasing depletion-attraction interactions. Likewise, the energetic barriers decrease as the nanoplate occupies a smaller volume fraction within the domain ($\approx 1.3\ k_BT \rightarrow \approx 1.0\ k_BT \rightarrow \approx 0.6\ k_BT$). The overall trend of energetic wells and barriers is analogous to the 5kPEG systems.

Our final analysis for this computational section reflects on the average PEG chain extension from the center of a given nanoplate toward the PS/PMMA interface (only the grafts extending in the positive x-direction (defined as away from the right side of the nanoplate, perpendicular to the PS/PMMA interface) are examined for the top nanoplate due to the inherent double mirror symmetry of the system as shown in Figure 2). Because one end of the chain is tethered to the nanoplate, we use the center of mass of the grafted chain from the center of the nanoplate as a proxy for the chain extension. Note that the high grafting density forces the chains to exist as extended brushes rather than as combs. The extension provides insight into the compression of the grafted chain caused by the diblock interface and, thus, the interplay between molecular weights of the graft and the matrix. We calculate the extension via

$$\left\langle x \right\rangle = \int_0^{L_x/2} x \cdot \rho_g(x)\, dx \Big/ \int_0^{L_x/2} \rho_g(x)\, dx \quad (1)$$

where the center of the x-dimension of the simulation cell (and of the nanoplate) has been defined as 0 and the right edge of the simulation cell has been defined as $L_x/2$. As seen in Table 3, for both graft lengths, the grafted chain extension shrinks as the matrix molecular weight decreases, with the centers of mass for both grafts moving closer to the nanoplate surface, though the changes are all small in magnitude. Figure S1 plots the distribution of the PS and PMMA density profiles for the 5kPEG systems (i) far away from the particles, (ii) between the two nanoparticles in the center of the box, and (iii) sliced horizontally through the center of the top nanparticle.

Table 3. Average Graft Chain Extension (nm) in the Positive x-Direction from the Center of the Top Nanoplate, with the Nanoplates at Their Energetic Minima[a]

	BCP Matrix MW		
Graft length	38kBCP	95kBCP	133kBCP
5kPEG	4.21	4.26	4.26
10kPEG	5.59	5.70	5.71

[a]Average chain extension ($\langle x \rangle$) is calculated from the center of the nanoplate by $\int_0^{L_x/2} x \cdot \rho_g(x)\, dx \Big/ \int_0^{L_x/2} \rho_g(x)\, dx$.

Experimental System and Comparison. Three representative TEM images are shown in Figure 5, one for each of the different matrix molecular weights, all with a graft length of 5 kg/mol PEG (only graft lengths of 5 kg/mol PEG were used in our experiments). For our computational work, we had assumed the nanoparticles themselves were perfectly aligned within the lamellar system. Experimentally, there is a degree of

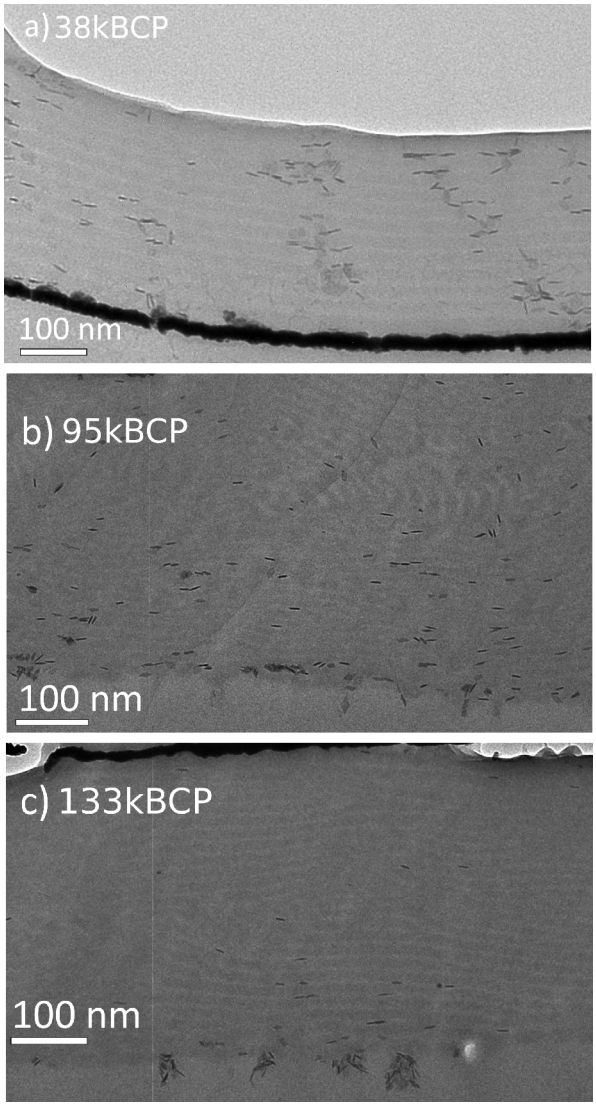

Figure 5. Representative TEM (JEM-1400, 120 kV) images of ultramicrotome lamellar-forming (a) 38kBCP, (b) 95kBCP, and (c) 133kBCP films with ϕ = 0.017 5kPEG functionalized nanoplates. The light domain is PMMA, and the dark domain is PS. Note: the dark feature lining the films is the Au/Pd tracer layer and indicates the top surface of the films. The top image is republished data from our previous paper.[40]

https://doi.org/10.1021/acs.macromol.1c02478
Macromolecules 2022, 55, 3166−3175

tilt between the nanoparticles themselves and the host matrix. Our previous work found the energetic penalty for particles tilted less than 5° to be less than 0.2 k_BT. (Particles oriented 10° have an additional 0.75 k_BT compared to the perfectly parallel particles.) As one can see, the nanoplates in the 95kBCP matrix (Figure 5b) appear on average to be more separated than the nanoplates found in the 38kBCP matrix (Figure 5a) but not as separated as in the 133k BCP matrix (Figure 5c).

To quantify this trend, we measured the end-to-end distances between 300 nearest neighbor nanoplates and created histograms of the distances in Figure 6 (details are

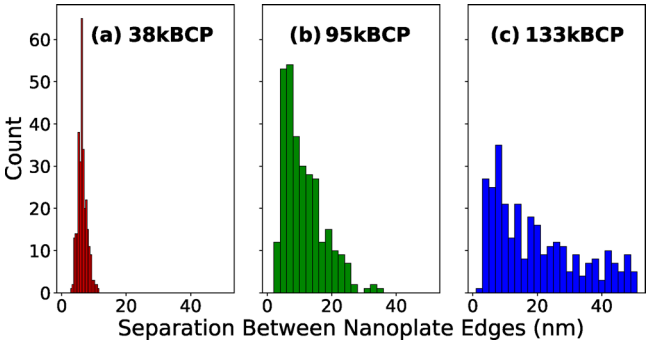

Figure 6. Histograms of experimentally measured separations between edges of 5kPEG functionalized GdF3:Yb/Er rhombic nanoplates that are aligned in the PMMA domain of lamellar-forming (a) 38kBCP, (b) 95kBCP, and (c) 133kBCP films. The bin size is set to 0.5 nm for the 38kBCP composite system since the nanoplates are more closely spaced than in the 95kBCP and 133kBCP matrices. The bin size is 2 nm for both the 95kBCP and 133kBCP composite systems.

available in the Supporting Information). The mean nanoplate separation distances were, in increasing matrix molecular weight, 6.4, 11.3, and 19.8 nm; the corresponding standard deviations were 1.4, 6.2, and 13.6 nm (see Table 4). For

Table 4. Statistics Regarding the Experimental Separation Distance

system ID	μ (mean) (nm)	σ (std) (nm)
38kBCP−5kPEG	6.4	±1.4
95kBCP−5kPEG	11.3	±6.2
133kBCP−5kPEG	19.8	±13.6

38kBCP, because the nanoplates are much closer together, the bin size was 0.5 nm; for the larger molecular weights, a bin size of 2 nm was employed, which provided a smoother representation of the data. If we assume the system has achieved equilibrium, the log of the probability (P) of two nanoplates having a certain separation distance is related to the Helmholtz free energy of the system (F) via

$$\frac{F}{k_BT} = -\ln P - \frac{F_0}{k_BT} \quad (2)$$

where k_B is the Boltzmann constant, T is the temperature of the system, and F_0 is a constant offset in the free energy; because we are interested in how the energy changes as a function of interplate distance, we set F_0 to 0. These histograms corroborate the visual inspection: the larger the molecular weight, the more distributed (and further distributed) the nanoplates become. Figure 7 shows the transformation of the histogram distributions into free energy profiles, where for the smaller molecular weight the nanoplates are located closer together and feature a narrower well than the other molecular weights. As the matrix molecular weight increases, the energetic minima ($\sim 4k_BT$) occur at roughly the same separation but have a noticeably wider energetic well. This well width simply reflects the increasing nanoplate separation as BCP molecular weight increases. Because of the limits of our sampling and the limited data from hand-counting nanoplate distances, we are unable to provide sufficient statistics to resolve the energetic barriers that might exist in the experimental system.

Comparing the simulation PMF in Figure 4a to the experimental PMF in Figure 7, we note that the two plots share many common features. Both sets of free energy profiles have a sharp energetic penalty at very close distances, similar depths for their asymmetric energy wells, and a widening of the energetic well as the molecular weight increases. While we are unable to resolve what the exact minima might be for the experimental systems, one can see a slight increase in the approximate location of the minima, matching the shift of the minima seen in the simulation system and strongly tying together the simulation and experimental results.

CONCLUSIONS

For nanoplates in a lamellar forming block copolymer, we investigated the effects of nanoplate graft length and block copolymer chain length on the system using hybrid particle/self-consistent field theory simulations and corroborated these results with select experimental systems. Simulations model the assembly of nanoplates functionalized with polyethylene glycol (PEG) having graft lengths of 5 kg/mol and 10 kg/mol incorporated into nearly symmetric ($f \approx 0.5$) polystyrene-b-poly(methyl methacrylate) (PS-b-PMMA) having block molecular weights of 38 kg/mol, 95 kg/mol, 133 kg/mol. The potential of mean force was calculated to show how free energy depends on the separation between nanoplates.

We discovered the energetic minima are highly dependent upon the relative volume fraction of grafted nanoplates to the lamellar domain. Our PS-b-PMMA with the narrowest domain exhibited the largest and most significant difference between the shorter and longer PEG grafts. Namely, the longer graft not only had a deeper well in the potential of mean force and a significantly larger energetic barrier than the shorter graft but also larger distortions in the density profiles at the PS/PMMA interface. The magnitude of the energetic well and maxima both decreased when the relative volume fraction of the nanoplate decreased, whether through the graft length reduction or through a dilation of the domain. This behavior is attributed to the energetic restrictions that prevents grafts from exploring more configurations as well as the general displacement of the BCP matrix caused by the nanoplate insertion explain the aforementioned chains. Importantly, this restriction of the graft configurations within the BCP domain changes the equilibrium spacing between nanoplates.

Simulations are compared to experimentally measured separations between PEG-grafted nanoplates which corroborate the correlation found in the simulations between larger matrix domains and a broadening of the energetic well. Experimentally, the average interplate separation shows a broadening as BCP molecular weight increases in good agreement with the simulation results.

https://doi.org/10.1021/acs.macromol.1c02478
Macromolecules 2022, 55, 3166−3175

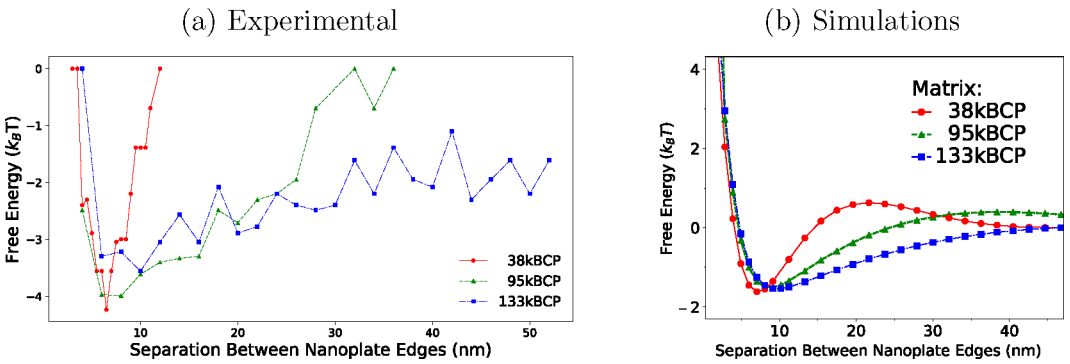

Figure 7. (a) Experimental free energy as a function of nanoplate edge-to-edge separation calculated for the 38kBCP, 95kBCP, and 133kBCP BCP matrices containing ϕ = 0.017 5kPEG functionalized nanoplates by normalizing results in Figure 6 over the total number of data points (300) to relate probability to energy using a Boltzmann distribution. (b) A reproduction of the inset from Figure 4a. Potential of mean force (PMF) curve near the energetic minima describing free energy as a function of edge-to-edge separation for 5kPEG-grafted nanoplates in the PMMA domain of PS-b-PMMA lamellae for various matrix molecular weights. 38kBCP is colored red, 95kBCP is green, and 133kBCP is blue.

Our findings can guide the design of future materials that fully exploit the unique properties of anisotropic polymer nanocomposites, specifically how to control the nanoplate distance, interplate distribution as well as the magnitude of the energetic well and barriers. In particular, nanoplate alignment and spacing will allow for improved performance of barrier materials used to reduce food spoilage as wel as coating to enhance photovoltaic device efficiency.

METHODS

hSCFT Simulations. We simulated the interactions of two grafted nanoplates within our lamellar polymer matrix. All chain lengths for a given polymer type are constant for each set of simulations, and our simulations have no polydispersity. By constricting the nanoplates within the lamellar domain and orienting the plates to approach each other edge-on, we mimic the way two experimental grafted nanoplates would interact. The simulations, while in two dimensions, were able to capture the general trends of our real-world experimental system, as demonstrated in our previous paper.[40] The specific model used allows us to easily calculate the free energy of the system while also providing a visualization of the equilibrium configuration of the system at each interplate separation distance; we have chosen our simulations' properties and dimensions to be able to compare trends of the simulation results against experimental systems. Nonvarying parameters of the model are described in the subsection Description of the Simulations while the variable parameters (including degree of polymerization, box dimensions, and the various χ's) can be found in Table 1. Note that we assume that any direct nanoparticle−polymers are neutral, with only incompressibility interactions between them. Representative visualizations of the energetic minima for each system are in Figure 2. The visualizations were made using the plotnine package for Python.[43]

Description of the Simulations. The simulation technique is identical to that of our previous paper,[40] which is based off previous hybrid particle/self-consistent field theory (hSCFT) implementations;[46−54] we include only the most relevant parts for the reader.

The polymers chains themselves, denoted herein as *A*, *B*, and *G*, are represented as discrete Gaussian chains of segment size *b* with a Gaussian bonding potential

$$\beta U_{\text{bond}} = \sum_{\{i,j\}} \frac{3\,|\mathbf{r}_i - \mathbf{r}_j|^2}{2} \tag{3}$$

where $\{i, j\}$ represents all unique bonds in the system. The nanoparticles are repulsive cavity functions expelling the polymer chains from their given region and have the following functional form:

$$\Gamma(\mathbf{r}) = \frac{\rho_0}{4}\,\text{erfc}\left(\frac{\left|\mathbf{u}\cdot(\mathbf{r}-\mathbf{r}_c)\right| - \frac{L_p}{2}}{\xi}\right) \text{erfc}\left(\frac{|\mathbf{u}\times(\mathbf{r}-\mathbf{r}_c)| - R_p}{\xi}\right) \tag{4}$$

where the R_p and L_p are the radius and length of the nanoparticle, respectively; the orientation and the center of the nanoparticle, $\mathbf{u}$ and $\mathbf{r}_c$, are fixed for each separate simulation; · represents a dot product; × represents a cross-product; the two erfc functions are multiplied with each other; the transition of the nanoparticle density from ρ_0 to 0 is controlled by the nanoparticle "width", denoted as ξ. Smaller values of ξ feature a sharper gradient but require a finer grid resolution, which increases computational cost.

The tethered ends of the grafted polymer chains are most heavily located at the nanoparticle "edge" and have a normalized probability distribution based off the gradient of the nanoparticle density:

$$\sigma(\mathbf{r}) = \frac{|\nabla\Gamma(\mathbf{r})|}{\int \mathbf{dr}|\nabla\Gamma(\mathbf{r})|} \tag{5}$$

The nonbonded interactions are comprised of two distinct contributions: Flory−Huggins potential (often thought of as polymer repulsion/dissimilarity) and the Helfand compressibility potential, which penalizes density fluctuations away from the average or "bulk" density ρ_0 to enforce a homogeneous total density profile. The Flory−Huggins potential has a simple local form as given by

$$\beta U_{\text{nb}} = \frac{\chi}{\rho_0}\int \mathbf{dr}\,\hat{\rho}_\alpha(\mathbf{r})\hat{\rho}_\beta(\mathbf{r}) \tag{6}$$

where χ governs the strength of the chemical repulsion (or chemical attraction if $\chi < 0$) between any of the three polymer types $\{A, B, G\}$. The Helfand potential takes the following functional form:[55]

$$\beta U_{\text{Helf}} = \frac{\kappa}{2\rho_0}\int \mathbf{dr}\,[\hat{\rho}_+(\mathbf{r}) - \rho_0]^2 \tag{7}$$

where ρ_+ represents the sum of all density fields, and κ is a prefactor controlling the penalty for density fluctuations. As κ tends toward infinity, our model recovers the incompressibility constraint of similar self-consistent field theory models. In our simulations, *A* is PS, *B* is PMMA, and *G* is the grafted PEG. The fields are updated using a semi-implicit Euler update scheme.

Numerical Parameters. To simplify calculations, we altered the nearly symmetric molecular weight composition of the diblocks to create symmetric amounts of A and B statistical monomeric units in our simulations. The 38k-b-36.8k g/mol system is represented as 38k-

https://doi.org/10.1021/acs.macromol.1c02478
Macromolecules 2022, 55, 3166−3175

b-36.625k g/mol, 95k-b-95k g/mol as 95k-b-91.35k g/mol, and 133k-b-130k g/mol as 133k-b-127.9k g/mol.

Our method is unchanged from our last paper.[40] Since the simulations are 2D, we represent the rhombic nanoplates as 2D rods; this can be thought of as a side-on projection. The third dimension is assumed to be uniform which corresponds to a simulation of infinite depth (when looking at the projection as done in Figure 2). Using the results from Eitouni and Balsara,[44] we set the statistical equivalent number of monomers and statistical segment size for our real-world polymers, which was then used to calculate the squared radius of gyration R_g^2. To determine the values of the parameters necessary for the simulations (namely, the statistical segment length and number of monomers per statistical segment), we took the simple average of the physical properties (monomer volume, statistical segment length) between the PS and PMMA blocks. Standardizing the statistical segment length b to roughly 2.322 nm allowed for comparisons across the various molecular weights.

The degree of polymerization of each block of the matrix is, in increasing molecular weight, 30, 75, and 105. The graft length of 5 kg/mol is modeled using 9 statistical beads and the 10 kg/mol is represented as 16 monomers. One statistical bead represents about 12 monomer units of the BCP chains and about 14 monomer units of the grafted PEG. To generate the potential of mean force (PMF) figures, the box width and height were chosen to be the smallest possible size while excluding any significant box size effects. The nanoparticle transition length (ξ) was set to 0.2 b units. The exact parameters for each simulation are outlined in Table 1. For all simulations, κ was set to 50 to equilibrate relatively quickly while having negligible effects on the final configurations. The thickness of the 3D plates is the diameter of the 2D rod and is 1.2918b units to align with the experimental 3 mm thickness. The diameters of the rhombus (d_1 = 35 mm, d_2 = 21 mm) are averaged together to obtain the length of the 2D nanoparticle (6.1318 b). We also map the experimental grafting density of 0.62 chains/nm^2 to 3.34 chains/b^2.

Potential of Mean Force Curves. Potential of mean force (PMFs) curves examine how the free energy changes with respect to one variable (in this case, the interplate distance). For our simulations, the reference state ($F_0 = 0\ k_BT$) is defined as the furthest possible state the nanoplates can be from each other in the simulation box while remaining constrained within the same lamellar domain while in the edge-on configuration. The vertical box size was iteratively enlarged until the nanoplate-nanoplate interactions were negligible at the reference state. The edge-to-edge distance between the nanoplates (oriented parallel to the matrix domains) was systematically reduced until the nanoplates overlapped with each other; we present distances without unphysical nanoplate-nanoplate overlap. The method we used to calculate the PMFs for experimental system is covered in the subsection "Experimental System and Comparison." The figures were generated using the matplotlib package for Python.[45]

Materials. The experimental molecular weights used were (1) M_n = 38k-b-36.8k g/mol (PDI = 1.08), (2) M_n = 95k-b-95k g/mol (PDI = 1.18), and (3) M_n = 133k-b-130k g/mol (PDI = 1.15) lamellar-forming poly(styrene-b-methyl methacrylate) (PS-b-PMMA) block copolymers (BCPs), which have been referred to throughout the paper as 38kBCP, 95kBCP, and 133kBCP, respectively. As mentioned earlier, the 38kBCP with 5kPEG system was originally studied in our previous paper.[40] The listed chemicals and polymers were used as received without further purification or modification. Toluene [99.9%, for high-performance liquid chromatography (HPLC)] was purchased from Sigma-Aldrich and hydrogen peroxide (H_2O_2, 30%, certified ACS), sodium hydroxide solution (NaOH, 50% w/w, certified), and sulfuric acid (H_2SO_4, certified ACS plus) were purchased from Fisher Scientific. EpoxiCure 2 epoxy hardener and epoxy resin were both purchased from Buehler. P-type, ⟨100⟩ oriented silicon (Si) wafers (dopant B, 0.001−0.005 Ω cm resistivity, 500 μm thickness, single side polished) with a 300 nm wet thermal oxide layer were purchased from University Wafer. The M_n = 95k-b-95k g/mol (PDI = 1.18) and the M_n = 133k-b-130k g/mol (PDI = 1.15) lamellar-forming poly(styrene-b-methyl methacrylate) (PS-b-PMMA) block copolymers (BCPs), selected as the matrix materials for the experimental studies, were purchased from Polymer Source Inc.

The related materials list and procedure for the rapid thermal decomposition synthesis of oleic acid (OA)-stabilized GdF3:Yb/Er (20/2 mol %) rhombic nanoplates [longest diagonal (d_1) = 35 nm, shortest diagonal (d_2) = 22 nm, and thickness (t) = 3 nm] was previously published.[56] Similarly, the solution phase ligand exchange and subsequent purification to functionalize the nanoplates with σ = 0.62 chains/nm^2 of phosphoric-acid-functionalized poly(ethylene glycol) (PEG−PO_3H_2, M_n = 5 kg/mol), purchased from Nanocs Inc., was previously reported.[56] The PEG−PO_3H_2-functionalized nanoplates were dispersed in toluene as a stock solution until incorporation into the BCP matrices. When discussing both the experiments and the simulations, the authors will refer to the M_n = 5 kg/mol grafted PEG−PO_3H_2 as 5kPEG. A M_n = 10 kg/mol PEG-grafted nanoplate was also simulated and is represented as 10kPEG. This molecular weight ligand was not available for purchase to study experimentally and will, therefore, only be discussed through calculations.

Block Copolymer Nanocomposite Preparation. Silicon wafers with a 300 nm wet thermal oxide layer were cut to 1 cm^2 and were subsequently cleaned in piranha solution (70:30 vol%, H_2SO_4:H_2O_2) at 80 °C for 20 min, rinsed three times with deionized water (DI H_2O), soaked overnight in DI H_2O, and dried the next day under N_2 flow. After piranha-cleaning, the Si substrates were treated with UV ozone for 10 min. Meanwhile, to form the polymer nanocomposite films, 5kPEG functionalized GdF_3:Yb/Er nanoplates were added from the concentrated stock solution to 1 wt % 95kBCP and 133kBCP in toluene at 40 °C. The polymer nanocomposite solutions were stirred with a magnetic stir bar for at least 2 h at 40 °C until the polymer was dissolved and the particles were dispersed. Once fully incorporated, 50 μL of the solutions were drop-casted onto the cleaned Si substrates (1 cm^2) and allowed to slowly evaporate over 48 h in a saturated toluene environment. Following a 24 h vacuum drying step, the films were thermally annealed under vacuum at 190 °C for 48 h. In the dry films, the final nanoplate volume fraction was ϕ = 0.017. With PMMA preferentially wetting the Si substrate, lamellae oriented parallel to the substrate surfaces were formed.

Transmission Electron Microscopy (TEM) and Images Analysis. TEM characterization was performed with a JEOL-1400 TEM operated at 120 kV. To prepare the samples for cross-sectional TEM imaging, the sample edges were scored around the perimeter and floated on the surface of a 40 °C NaOH solution (80:20 vol %, DI H_2O:50% w/w NaOH solution). Once the NaOH solution etched away at the 300 nm wet thermal oxide layer, the films floated away from the substrates and were suspended at the liquid−air interface. The floated polymer nanocomposite films were transferred to and rinsed in DI H_2O before deposited onto Teflon. After DI H_2O evaporation, the top of the BCP nanocomposite surfaces were sputter-coated with a gold (Au) and palladium (Pd) layer, lifted from the Teflon, and embedded in two-part epoxy. Cross sections (∼ 50−70 nm thick) were cut by ultramicrotomy (Leica Ultracut S Ultramicrotome) with a diamond knife and deposited onto carbon-coated TEM grids for imaging. For each BCP-based nanocomposite system, 300 edge-to-edge distances between NPs were measured using ImageJ (v 1.52a) analysis. The process to determine these separation distances was previously described.[40] All 300 measurements extracted from the images of ϕ = 0.017 5kPEG grafted nanoplates in 95kBCP and 133kBCP are listed in Table S1 and Table S2, respectively. The 300 measurements extracted from the images of 5kPEG grafted nanoplates in 38kBCP are reproduced from our previous paper[40] in Table S3. A characteristic example of the analysis can be found in Figure S4 of the Supporting Information of Krook et al.[40] Note that the analysis draws a straight line through the particles regardless of their orientation.

https://doi.org/10.1021/acs.macromol.1c02478
Macromolecules 2022, 55, 3166−3175

■ ASSOCIATED CONTENT

Supporting Information

The Supporting Information is available free of charge at https://pubs.acs.org/doi/10.1021/acs.macromol.1c02478.

Table of the 300 measured NP separation values for each experimental system and scaled measurements of PS and PMMA densities for 5kPEG systems (PDF)

■ AUTHOR INFORMATION

Corresponding Authors

Russell J. Composto − *Department of Materials Science and Engineering, University of Pennsylvania, Philadelphia, Pennsylvania 19104, United States;* orcid.org/0000-0002-5906-2594; Email: composto@seas.upenn.edu

Robert A. Riggleman − *Department of Chemical Engineering, University of Pennsylvania, Philadelphia, Pennsylvania 19104, United States;* orcid.org/0000-0002-5434-4787; Email: rrig@seas.upenn.edu

Authors

Christian Tabedzki − *Department of Chemical Engineering, University of Pennsylvania, Philadelphia, Pennsylvania 19104, United States;* orcid.org/0000-0001-8409-6094

Nadia M. Krook − *Department of Materials Science and Engineering, University of Pennsylvania, Philadelphia, Pennsylvania 19104, United States;* Present Address: DuPont Co., Wilmington, Delaware 19803, United States; orcid.org/0000-0003-3308-9040

Christopher B. Murray − *Department of Chemistry, University of Pennsylvania, Philadelphia, Pennsylvania 19104, United States*

Complete contact information is available at: https://pubs.acs.org/10.1021/acs.macromol.1c02478

Author Contributions

⊥C.T. and N.M.K. contributed equally to this work.

Notes

The authors declare no competing financial interest.

■ ACKNOWLEDGMENTS

The authors acknowledge funding from the National Science Foundation with support from the POLYMERS-DMR-1507713 and 1905912 (N.M.K., R.J.C.), PIRE-OISE-1545884 (N.M.K., C.T., C.B.M., R.A.R., and R.J.C.), and MRSEC-DMR-1720530 (N.M.K., C.B.M., and R.J.C.) programs as well as partial support from ANR-15-PIRE-0001-07. Computational support from the Extreme Science and Engineering Discovery Environment is gratefully acknowledged through award TG-DMR150034. The authors thank Dr. Karen I. Winey for use of the ultramicrotome and vacuum furnaces in her laboratory. The authors are also grateful for helpful discussions with Dr. Debra Audus, Dr. Shawn M. Maguire, Michael J. Boyle, Dr. Benjamin J. Lindsay, and Zachariah Vicars.

■ REFERENCES

(1) Kolate, A.; Baradia, D.; Patil, S.; Vhora, I.; Kore, G.; Misra, A. PEG — A versatile conjugating ligand for drugs and drug delivery systems. *J. Controlled Release* **2014**, *192*, 67−81.

(2) Greenwald, R. B.; Choe, Y. H.; McGuire, J.; Conover, C. D. Effective drug delivery by PEGylated drug conjugates. *Adv. Drug Delivery Rev.* **2003**, *55*, 217−250.

(3) Veronese, F. M.; Pasut, G. PEGylation, successful approach to drug delivery. *Drug Discovery Today* **2005**, *10*, 1451−1458.

(4) Grossen, P.; Witzigmann, D.; Sieber, S.; Huwyler, J. PEG-PCL-based nanomedicines: A biodegradable drug delivery system and its application. *J. Controlled Release* **2017**, *260*, 46−60.

(5) DiPalma, J. A.; Cleveland, M. B.; McGowan, J.; Herrera, J. L. A Comparison of Polyethylene Glycol Laxative and Placebo for Relief of Constipation From Constipating Medications. *Southern Medical Journal* **2007**, *100*, 1085−1090.

(6) Choi, J.; Koo, H.; Kim, T.; Choi, D.; Hayk, K. Rollable Display Device, Patent US 2020337161 A1, 2020.

(7) Rahman, M. M.; Filiz, V.; Khan, M. M.; Gacal, B. N.; Abetz, V. Functionalization of POSS nanoparticles and fabrication of block copolymer nanocomposite membranes for CO2 separation. *React. Funct. Polym.* **2015**, *86*, 125−133.

(8) You, I.; Kong, M.; Jeong, U. Block Copolymer Elastomers for Stretchable Electronics. *Acc. Chem. Res.* **2019**, *52*, 63−72.

(9) Fazlina Osman, A.; Rasyidah Abdul Hamid, A.; Fareyhynn Mohammed Fitri, T.; Amalia Ahmad Fauzi, A.; Anwar Abdul Halim, K. Poly(ethylene-co-vinylacetate) Copolymer Based Nanocomposites: A Review. *IOP Conference Series: Materials Science and Engineering* **2020**, *864*, 012121.

(10) Boaretto, N.; Meabe, L.; Martinez-Ibañez, M.; Armand, M.; Zhang, H. Review—Polymer Electrolytes for Rechargeable Batteries: From Nanocomposite to Nanohybrid. *J. Electrochem. Soc.* **2020**, *167*, 070524.

(11) Terzić, I.; Meereboer, N. L.; Mellema, H. H.; Loos, K. Polymer-based multiferroic nanocomposites: Via directed block copolymer self-assembly. *Journal of Materials Chemistry C* **2019**, *7*, 968−976.

(12) Chen, J.; Huang, X.; Sun, B.; Wang, Y.; Zhu, Y.; Jiang, P. Vertically Aligned and Interconnected Boron Nitride Nanosheets for Advanced Flexible Nanocomposite Thermal Interface Materials. *ACS Appl. Mater. Interfaces* **2017**, *9*, 30909.

(13) Hung, M.-T.; Choi, O.; Ju, Y. S.; Hahn, H. T. Heat conduction in graphite-nanoplatelet-reinforced polymer nanocomposites. *Appl. Phys. Lett.* **2006**, *89*, 023117.

(14) Novakova, A.; Lanchinskaya, V.; Volkov, A.; Gendler, T.; Kiseleva, T.; Moskvina, M.; Zezin, S. Magnetic properties of polymer nanocomposites containing iron oxide nanoparticles. *J. Magn. Magn. Mater.* **2003**, *258*−*259*, 354−357.

(15) Wilson, J. L.; Poddar, P.; Frey, N. A.; Srikanth, H.; Mohomed, K.; Harmon, J. P.; Kotha, S.; Wachsmuth, J. Synthesis and magnetic properties of polymer nanocomposites with embedded iron nanoparticles. *J. Appl. Phys.* **2004**, *95*, 1439−1443.

(16) Millan, A.; Palacio, F.; Falqui, A.; Snoeck, E.; Serin, V.; Bhattacharjee, A.; Ksenofontov, V.; Gütlich, P.; Gilbert, I. Maghemite polymer nanocomposites with modulated magnetic properties. *Acta Mater.* **2007**, *55*, 2201−2209.

(17) Sanporean, C.-G.; Vuluga, Z.; Radovici, C.; Panaitescu, D. M.; Iorga, M.; Christiansen, J. d.; Mosca, A. Polypropylene/organoclay/SEBS nanocomposites with toughness−stiffness properties. *RSC Adv.* **2014**, *4*, 6573.

(18) Sakakibara, K.; Moriki, Y.; Yano, H.; Tsujii, Y. Strategy for the Improvement of the Mechanical Properties of Cellulose Nanofiber-Reinforced High-Density Polyethylene Nanocomposites Using Diblock Copolymer Dispersants. *ACS Appl. Mater. Interfaces* **2017**, *9*, 44079−44087.

(19) Zhao, Y.; Thorkelsson, K.; Mastroianni, A. J.; Schilling, T.; Luther, J. M.; Rancatore, B. J.; Matsunaga, K.; Jinnai, H.; Wu, Y.; Poulsen, D.; Fréchet, J. M. J.; Paul Alivisatos, A.; Xu, T. Small-molecule-directed nanoparticle assembly towards stimuli-responsive nanocomposites. *Nat. Mater.* **2009**, *8*, 979−985.

(20) Listak, J.; Bockstaller, M. R. Stabilization of Grain Boundary Morphologies in Lamellar Block Copolymer/Nanoparticle Blends. *Macromolecules* **2006**, *39*, 5820−5825.

(21) Kutvonen, A.; Rossi, G.; Puisto, S. R.; Rostedt, N. K. J.; Ala-Nissila, T. Influence of nanoparticle size, loading, and shape on the mechanical properties of polymer nanocomposites. *J. Chem. Phys.* **2012**, *137*, 214901.

(22) Kutvonen, A.; Rossi, G.; Ala-Nissila, T. Correlations between mechanical, structural, and dynamical properties of polymer nanocomposites. *Phys. Rev. E* **2012**, *85*, 041803.
(23) Moll, J. F.; Akcora, P.; Rungta, A.; Gong, S.; Colby, R. H.; Benicewicz, B. C.; Kumar, S. K. Mechanical reinforcement in polymer melts filled with polymer grafted nanoparticles. *Macromolecules* **2011**, *44*, 7473−7477.
(24) Boo, W. J.; Sun, L.; Liu, J.; Moghbelli, E.; Clearfield, A.; Sue, H.-J.; Pham, H.; Verghese, N. Effect of nanoplatelet dispersion on mechanical behavior of polymer nanocomposites. *J. Polym. Sci., Part B: Polym. Phys.* **2007**, *45*, 1459−1469.
(25) Akcora, P.; Liu, H.; Kumar, S. K.; Moll, J.; Li, Y.; Benicewicz, B. C.; Schadler, L. S.; Acehan, D.; Panagiotopoulos, A. Z.; Pryamitsyn, V.; Ganesan, V.; Ilavsky, J.; Thiyagarajan, P.; Colby, R. H.; Douglas, J. F. Anisotropic self-assembly of spherical polymer-grafted nanoparticles. *Nat. Mater.* **2009**, *8*, 354−359.
(26) Xu, G.-K.; Feng, X.-Q.; Yu, S.-W. Controllable nanostructural transitions in grafted nanoparticle-block copolymer composites. *Nano Research* **2010**, *3*, 356−362.
(27) Gao, K.; Wan, H.; Tsen, E. J. L.; Liu, J.; Lyulin, A. V.; Zhang, L. Unveiling the Mechanism of the Location of the Grafted Nanoparticles in a Lamellar-Forming Block Copolymer. *Langmuir* **2020**, *36*, 194−203.
(28) Thorkelsson, K.; Mastroianni, A. J.; Ercius, P.; Xu, T. Direct nanorod assembly using block copolymer-based supramolecules. *Nano Lett.* **2012**, *12*, 498.
(29) Li, W.; Zhang, P.; Dai, M.; He, J.; Babu, T.; Xu, Y. L.; Deng, R.; Liang, R.; Lu, M. H.; Nie, Z.; Zhu, J. Ordering of gold nanorods in confined spaces by directed assembly. *Macromolecules* **2013**, *46*, 2241.
(30) Hsu, S.-W.; Xu, T. Tailoring Co-assembly of Nanodiscs and Block Copolymer-Based Supramolecules by Manipulating Interparticle Interactions. *Macromolecules* **2019**, *52*, 2833−2842.
(31) Kausar, A. Polymer/nanodisk nanocomposite: futuristic vision toward advanced materials. *Polymer-Plastics Technology and Materials* **2021**, *60*, 488−503.
(32) Porel, S.; Singh, S.; Radhakrishnan, T. P. Polygonal gold nanoplates in a polymer matrix. *Chem. Commun.* **2005**, *2387*, 2387.
(33) Chen, J.; Huang, X.; Sun, B.; Jiang, P. Highly Thermally Conductive Yet Electrically Insulating Polymer/Boron Nitride Nanosheets Nanocomposite Films for Improved Thermal Management Capability. *ACS Nano* **2019**, *13*, 337−345.
(34) Idumah, C. I.; Hassan, A. Recently emerging trends in thermal conductivity of polymer nanocomposites. *Reviews in Chemical Engineering* **2016**, *32*, DOI: 10.1515/revce-2016-0004.
(35) Bhunia, K.; Dhawan, S.; Sablani, S. S. Modeling the Oxygen Diffusion of Nanocomposite-based Food Packaging Films. *J. Food Sci.* **2012**, *77*, N29−N38.
(36) Emamifar, A.; Kadivar, M.; Shahedi, M.; Soleimanian-Zad, S. Evaluation of nanocomposite packaging containing Ag and ZnO on shelf life of fresh orange juice. *Innovative Food Science & Emerging Technologies* **2010**, *11*, 742−748.
(37) Rhim, J.-W.; Park, H.-M.; Ha, C.-S. Bio-nanocomposites for food packaging applications. *Prog. Polym. Sci.* **2013**, *38*, 1629−1652.
(38) Gholami, R.; Ahmadi, E.; Farris, S. Shelf life extension of white mushrooms (Agaricus bisporus) by low temperatures conditioning, modified atmosphere, and nanocomposite packaging material. *Food Packaging and Shelf Life* **2017**, *14*, 88−95.
(39) Bockstaller, M. R.; Mickiewicz, R. A.; Thomas, E. L. Block Copolymer Nanocomposites: Perspectives for Tailored Functional Materials. *Adv. Mater.* **2005**, *17*, 1331−1349.
(40) Krook, N. M.; Tabedzki, C.; Elbert, K. C.; Yager, K. G.; Murray, C. B.; Riggleman, R. A.; Composto, R. J. Experiments and Simulations Probing Local Domain Bulge and String Assembly of Aligned Nanoplates in a Lamellar Diblock Copolymer. *Macromolecules* **2019**, *52*, 8989−8999.
(41) Deshmukh, R. D.; Liu, Y.; Composto, R. J. Two-Dimensional Confinement of Nanorods in Block Copolymer Domains. *Nano Lett.* **2007**, *7*, 3662−3668.
(42) Garde, S.; Patel, A. J. Unraveling the hydrophobic effect, one molecule at a time. *Proc. Natl. Acad. Sci. U. S. A.* **2011**, *108*, 16491−16492.
(43) Kibirige, H. has2k1/plotnine: v0.8.0. *Zenodo*; 2021, DOI: 10.5281/ZENODO.4636791.
(44) Eitouni, H. B.; Balsara, N. P. *Physical Properties of Polymers Handbook*; Springer: New York, NY, 2007; pp 339−356, DOI: DOI: 10.1007/978-0-387-69002-5_19.
(45) Hunter, J. D. Matplotlib: A 2D Graphics Environment. *Computing in Science & Engineering* **2007**, *9*, 90−95.
(46) Sides, S. W.; Kim, B. J.; Kramer, E. J.; Fredrickson, G. H. Hybrid Particle-Field Simulations of Polymer Nanocomposites. *Phys. Rev. Lett.* **2006**, *96*, 250601.
(47) Rasin, B.; Chao, H.; Jiang, G.; Wang, D.; Riggleman, R. A.; Composto, R. J. Dispersion and alignment of nanorods in cylindrical block copolymer thin films. *Soft Matter* **2016**, *12*, 2177−2185.
(48) Matsen, M. W.; Thompson, R. B. Particle Distributions in a Block Copolymer Nanocomposite. *Macromolecules* **2008**, *41*, 1853−1860.
(49) Koski, J.; Chao, H.; Riggleman, R. A. Field theoretic simulations of polymer nanocomposites. *J. Chem. Phys.* **2013**, *139*, 244911.
(50) Hickey, R. J.; Koski, J.; Meng, X.; Riggleman, R. A.; Zhang, P.; Park, S.-J. Size-Controlled Self-Assembly of Superparamagnetic Polymersomes. *ACS Nano* **2014**, *8*, 495−502.
(51) Koski, J.; Chao, H.; Riggleman, R. a. Predicting the structure and interfacial activity of diblock brush, mixed brush, and Janus-grafted nanoparticles. *Chem. Commun.* **2015**, *51*, 5440−5443.
(52) Ferrier, R. C.; Lee, H.-S.; Hore, M. J. A.; Caporizzo, M.; Eckmann, D. M.; Composto, R. J. Gold nanorod linking to control plasmonic properties in solution and polymer nanocomposites. *Langmuir: the ACS journal of surfaces and colloids* **2014**, *30*, 1906−14.
(53) Koski, J.; Ferrier, R. C.; Krook, N. M.; Chao, H.; Composto, R. J.; Frischknecht, A. L.; Riggleman, R. A. Comparison of Field-Theoretic Approaches in Predicting Polymer Nanocomposite Phase Behavior. *Macromolecules* **2017**, *50*, 8797−8809.
(54) Hore, M. J.; Composto, R. J. Using miscible polymer blends to control depletion-attraction forces between Au nanorods in nanocomposite films. *Macromolecules* **2012**, *45*, 6078−6086.
(55) Helfand, E. Theory of inhomogeneous polymers: Fundamentals of the Gaussian random-walk model. *J. Chem. Phys.* **1975**, *62*, 999−1005.
(56) Krook, N. M.; Ford, J.; Maréchal, M.; Rannou, P.; Meth, J. S.; Murray, C. B.; Composto, R. J. Alignment of Nanoplates in Lamellar Diblock Copolymer Domains and the Effect of Particle Volume Fraction on Phase Behavior. *ACS Macro Lett.* **2018**, *7*, 1400−1407.

https://doi.org/10.1021/acs.macromol.1c02478
Macromolecules 2022, 55, 3166−3175